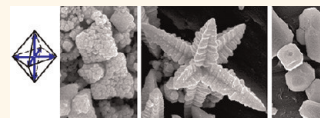# Unknown Aspects of Self-Assembly of PbS Microscale Superstructures

Ana Querejeta-Fernández,[†] Juan C. Hernández-Garrido,[‡] Hengxi Yang,[§] Yunlong Zhou,[†] Aurea Varela,[||] Marina Parras,[||] José J. Calvino-Gámez,[‡] Jose M. González-Calbet,[||] Peter F. Green,[⊥] and Nicholas A. Kotov[†,⊥,¶,*]

[†]Chemical Engineering Department, University of Michigan, Ann Arbor, Michigan 48109, United States, [‡]Departamento de Ciencias de Materiales, Ingeniería Metalúrgica y Química Inorgánica, Universidad de Cádiz, Puerto Real, 11510 Cádiz, Spain, [§]Physics Department and [⊥]Material Science and Engineering Department, University of Michigan, Ann Arbor, Michigan 48109, United States, [||]Departamento de Química Inorgánica I, Facultad de Ciencias Químicas, Universidad Complutense de Madrid, 28040 Madrid, Spain, and [¶]Biomedical Engineering Department, University of Michigan, Ann Arbor Michigan 48109, United States

Self-organization of nanoparticles (NPs) takes place for many materials.[1−7] Particularly diverse behavior and resulting geometries were observed for the self-assembly (SA) of semiconductor NPs. Their superstructures include straight nanowires (NWs),[8−10] zigzag NWs,[10] branched NWs,[10] nanorings,[10] nanochains,[11] nanocheck and X-marks,[12] nanosheets,[13] and even twisted ribbons.[14] While many of these examples involve pairwise interactions of NPs, which are increasingly better understood, the mechanisms of SA behavior for large NP ensembles and the driving forces for complex three-dimensional (3D) superstructures are still in its infancy. This field deserves a lot of additional attention since it can potentially reconfigure many technologies using simple and elegant SA manufacturing methods.[1,2,4,5] As such, SA processes can bridge nanoscale materials and well-established microscale technologies opening new architectures and functionalities of NEMS and MEMS devices. They can also lead to new mesocrystalline materials resembling biomineralization processes.[4,5,15] The interplay of different attractive/repulsive interactions between NP, ion exchange, and the physicochemical characteristics of the surrounding medium creates rich parameter space for nanoscale engineering of SA superstructures. From this perspective, one should also analyze the areas where the field of NP self-organization requires substantial advancements necessary for both technological and fundamental standpoints. The analysis of the current *status quo* indicates that much better understanding needs to be achieved for (a) mechanisms and driving forces of 3D SA with both nano- and microlevels of organization; (b) disassembly/deconstruction processes

ABSTRACT A lot of interesting and sophisticated examples of nanoparticle (NP) self-assembly (SA) are known. From both fundamental and technological standpoints, this field requires advancements in three principle directions: (a) understanding the mechanism and driving forces of three-dimensional (3D) SA with both nano- and microlevels of organization; (b) understanding disassembly/deconstruction processes; and (c) finding synthetic methods of assembly into continuous superstructures without insulating barriers. From this perspective, we investigated the formation of well-known star-like PbS superstructures and found a number of previously unknown or overlooked aspects that can advance the knowledge of NP self-assembly in these three directions. The primary one is that the formation of large seemingly monocrystalline PbS superstructures with multiple levels of octahedral symmetry can be explained only by SA of small octahedral NPs. We found five distinct periods in the formation PbS hyperbranched stars: (1) nucleation of early PbS NPs with an average diameter of 31 nm; (2) assembly into 100−500 nm octahedral mesocrystals; (3) assembly into 1000−2500 nm hyperbranched stars; (4) assembly and ionic recrystallization into six-arm rods accompanied by disappearance of fine nanoscale structure; (5) deconstruction into rods and cuboctahedral NPs. The switches in assembly patterns between the periods occur due to variable dominance of pattern-determining forces that include van der Waals and electrostatic (charge−charge, dipole−dipole, and polarization) interactions. The superstructure deconstruction is triggered by chemical changes in the deep eutectic solvent (DES) used as the media. PbS superstructures can be excellent models for fundamental studies of nanoscale organization and SA manufacturing of (opto)electronics and energy-harvesting devices which require organization of PbS components at multiple scales.

representing the inevitable opposite of SA that have been scarcely addressed;[11,14,16,17] and (c) practical methods of NP assembly into continuous superstructures without insulating organic barriers, making many applications in NEMS, MEMS, and electronic devices impossible.

Lead sulfide, PbS, represents a promising candidate for future studies of NP

self-organization potentially leading to implementation of optoelectronic (photovoltaic solar cells[16] and infrared emission/detection devices[17]) and thermoelectric[18,19] technologies. All three principle challenges mentioned above are equally applicable to PbS as well as other semiconductor and metal NPs. While it is very well-known that PbS forms hyperbranched nano/microstructures,[23−41] the mechanism of their formation leading to very intricate superstructures is not understood and can partially account for hyperbranched geometries only at nanometer scale.[18,20−27] What is also true is that SA has not been considered as the formation pathway.[28−39] The nature of driving forces involved in SA or deconstruction processes of PbS and other superstructures have not been addressed also. Understanding of the dualism of SA and deconstruction is essential to create a dynamic nanoscale and microscale system.[43]

Given that advanced optoelectronic applications demand the combination of nano- (beneficial in terms of charge carrier generation),[44−48] submicro- (required for efficient charge transport),[49,50] and mesoscale (significant for mechanical properties and scalability) levels of structural organization, controlled SA approach leading to hierarchical hyperbranched structures will allow fabrication of electronic devices based on PbS. However, the long-chain molecules previously used for assisting the synthesis of hyperbranched PbS structures create insulating gaps with high tunneling resistance, which is detrimental for the charge-transfer process at the interface between NPs.[51,52] Control over the internal porosity of PbS mesocrystals is also necessary for advancements in thermoelectrics.[18,19]

Given this background, we report here new findings about formation and evolution of PbS nano/microsuperstructures in a deep eutectic solvent (DES).[53] On the basis of extensive experimental data, we concluded that the growth of complex micrometer scale superstructures can only be explained *via* progressive assembly of octahedral NPs. Short chains of urea−choline chloride DES are advantageous for the SA of PbS compared to long-chain capping agents in organic and aqueous solvents considered before[2−7] due to formation of extended superstructures without insulating gaps. Five different stages of the assembly process have been identified. The interparticle forces determining the SA pattern in each stage and their switches between the stages are discussed. The appearance of the hierarchical hyperbranched geometry of the self-organized superstructures from PbS NPs is a result of the interplay of dipolar interactions and minimization of polarization energy. Decrease of polarity of DES upon urea decomposition is accompanied by the disassembly/deconstruction of the superstructures due to increased electrostatic repulsion. An increase in ion exchange processes and their effect
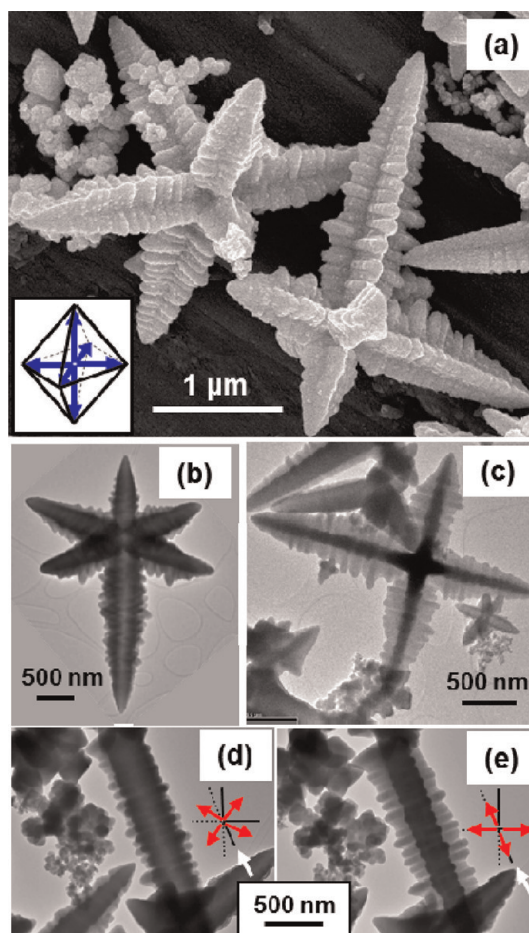

Figure 1. Hierarchical hyperbranched PbS crystals obtained at t_r = 30 min. (a) SEM image of hyperbranched stars. Inset shows the octahedral motif displayed at every level of hierarchy. (b,c) TEM images of two hyperbranched stars viewed along two perspectives. In (c) (orientation close to [001] zone axis), the projection of two main branches can be seen as the darker area in the center of the star. (d,e) TEM images of a same single-arm crystal.

on superstructure geometry is also observed at the later stages of the reaction.

RESULTS

Hyperbranched PbS Nano/Microcrystals in Deep Eutectic Solvents. DESs[53] with short chains can be a uniquely convenient medium for assembly of NPs because they combine the properties of both organic and inorganic solvents. DESs also provide quite unusual electrostatic conditions and intermolecular interactions for solutes, altering in many instances reaction pathways.[54−56] DESs share many properties with ionic liquids (ILs) including high polarity and supramolecular self-organization,[54−56] while providing additional advantages exemplified by biodegradability and synthetic simplicity. Although ILs and DESs seem to facilitate the formation of unusual geometries of dispersed particles[55,57,58] and low-dimensional solids,[59] their suitability for SA processes of NPs is still unknown.

After 30 min of combining the Pb^{2+} and S^{2-} precursors in hot DES, one can observe nano/microscale assemblies that can be described as 3D hyperbranched PbS microstars with multiple levels of hierarchy (Figure 1a−e). Additional products included small agglomerates of NPs and dendritic assemblies analogous to the single arms of the microstars (Figure S1 in Supporting Information). Each "star" has six main branches pointing to the six equivalent ⟨100⟩ directions of an imaginary octahedron (Figure 1c). Each main branch supports four perpendicular rows of secondary branches with a diameter of ∼50−150 nm, which will be referred to here for brevity as nanorods (NRs). The rows of the NRs can be seen as the fringes of the main branches and the darker central zone blocking electron beam in two tiers. Each NR possesses four perpendicular facets (Figure 1a). TEM tomography displays the geometrical features of the hyperbranched microstars particularly vividly (Figure 2a). Video files displaying the complex 3D structure are available in Supporting Information Figures SV2 and SV3.

The size of the NRs is larger than the Bohr radius of PbS (18 nm).[60] The degree of the quantum confinement in the superstructure must be very small approaching the band gap of PbS in the bulk (0.4 eV).[61] Interestingly, broad UV−vis absorbance peaks at 800−900 nm (Figure S4; note that the peak at 963 nm is from DES, not from PbS) point to the fact that the actual band gap for substantial portion of the superstructure is 1.5−1.3 eV. Such discrepancy must be related to nanoscale organization of the superstructure and, therefore, to the process of its formation. No band gap emission peak can be detected in the same region (Figure S5). Looking into the potential origin of the quantum confinement, we did not see obvious grain boundaries between the NRs as can be seen in the high-resolution TEM (HRTEM) images in Figure 3d−f. Selected area electron diffraction (SAED) data (Figure 3b) confirmed a seemingly single-crystalline nature of the hyperbranched stars. High crystallinity and atomic quality of interfaces minimizes scattering of charge carriers important for electronic applications.[62]

The growth of the branches occurs along the six equivalent ⟨100⟩ crystallographic directions, as well as the ⟨100⟩ directions of each secondary branch or NR (Figure 3). Insights into the internal organization of the hyperbranched microstars can be obtained from the three-dimensional (3D) images obtained by transmission electron tomography (Figure 2a and video files in Supporting Information SV2 and SV3), which reveals the presence of mesoscale pores in these structures. Furthermore, one can also detect the presence of NPs firmly attached to the surface of the structures (Figure S6). In aggregate, the spectroscopic and microscopy data indicate that a simple ion-by-ion growth mechanism cannot govern the formation of hyperbranched microstars. This mechanism can explain neither the
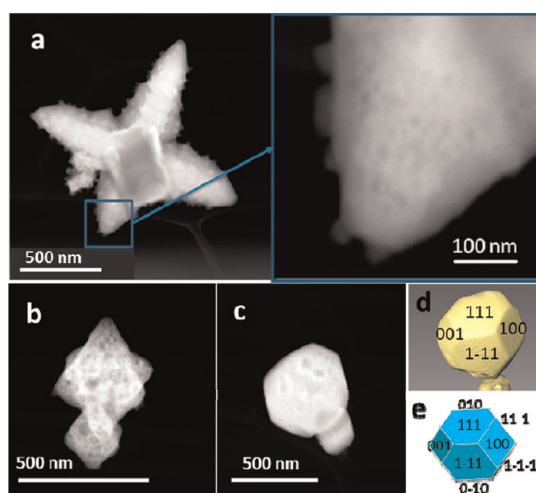

Figure 2. HAADF-STEM images of the PbS products obtained at different reaction times (t_r). (a) Hyperbranched PbS star obtained at t_r = 30 min showing internal porosity and NPs in close contact to the surface of the stars. (b) Octahedral porous mesocrystal obtained at t_r = 10 min. (c) PbS nanoparticle obtained at t_r = 5 days. Degree of porosity in the products increases in the order (b) t_r = 10 min > (a) t_r = 30 min > (c) t_r = 5 days. (d) Three-dimensional view of the PbS nanoparticle (c) reconstructed from a tilt series and (e) its proposed morphology, corresponding to a cuboctahedron-like polyhedral shape with its indexed {hkl} facets.
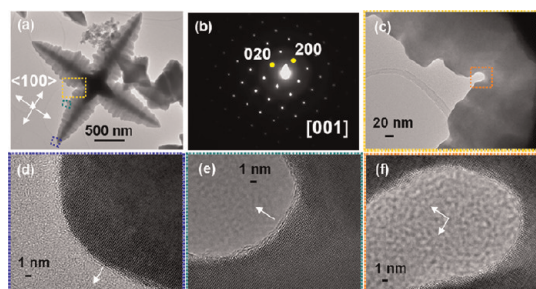

Figure 3. (a) TEM image of a PbS hyperbranched star obtained at t_r = 30 min. (b) Corresponding SAED pattern along the [001] zone axis. (c−f) TEM and HRTEM images of the highlighted areas in (a) showing the high crystallinity of the SA superstructure.
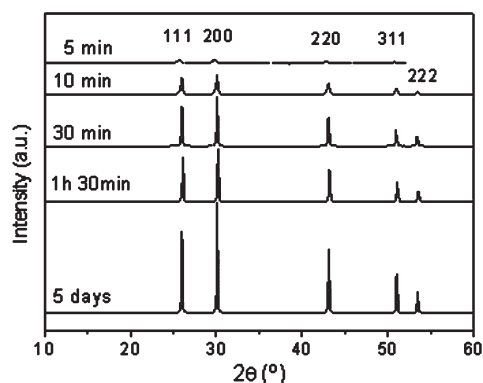

Figure 4. XRD patterns of the PbS (galena) products obtained at different reaction times.

presence of strong quantum confinement nor the presence of internal cavities.

Previous studies[24,27−39] correctly identified the uniqueness of PbS microstars' geometry but did not provide a consistent mechanism of their formation. Observation of related hierarchical PbS dendrites with one,[24,28,31,33,34] four,[28] and eight arms[23,29,30,35,36] demonstrated the ubiquitous nature of such superstructure but, again, shed little light on the mechanism. One can clearly see a general trend for the growth of PbS nanostructures in this particular architecture but cannot find the reasons for such spontaneously developing complexity or the reason why it occurs for PbS and not for ZnO, CdTe, CdS, or other materials.

Different Stages of PbS Assembly. As a part of the study of the growth mechanism, we decided to examine reaction products at different reaction times (t_r) for the same reaction batch. Corresponding X-ray diffraction (XRD) patterns (Figure 4) show the presence of crystalline PbS (galena) as the only product at all t_r ranging from 5 min to 5 days. The peak intensities increase with t_r, evidencing an increase of the crystal size at longer reaction times, which matches the TEM observations (Figure 5).

Let us divide the morphological changes of the PbS structures into five periods with five characteristic products: early NPs, octahedral mesocrystals, hyperbranched stars, their reorganization and loss of nanoscale complexity, and the final period and products of deconstruction. For the *first period*, TEM examination reveals the formation of relatively polydisperse octahedral NPs with an average diameter of 31.3 ± 10.7 nm (Figure S7) after 5 min of reaction (Figures 5 and 6a). They are monocrystalline and display galena lattice and interplanar distances (Figure 6c). During this period, we also see the tendency of the NPs to group. At this point, there is little registry between the crystal lattices of NPs in these loose agglomerates of NPs as can be seen in the characteristic ring pattern of SAED (Figure 6b).

During the *second period* with characteristic reaction time of $t_r = 10$ min, NP agglomeration becomes more pronounced and produces clusters of $\sim 100-500$ nm in diameter (Figure 5). Both SEM (Figure 7 and Figure S1 in Supporting Information) and HAADF-STEM images of the resulting mesocrystals (Figure 2b, tomography, and video in Figures S8a,b and SV9) reveal the familiar octahedral shapes but much larger in scale than those during the first period. The mesocrystals, also known as supraparticles, are made from imperfectly fused NPs. Despite that, the assemblies demonstrate the epitaxial match of crystal lattices at the interfaces by SAED and HRTEM (Figure S10, Supporting Information). The vertexes of the octahedron are oriented along the six equivalent ⟨100⟩ directions. Angle-resolved HAADF-STEM images (Figure S8a,b, Supporting Information) and the video from the 3D reconstruction (Figure SV9, Supporting Information) clearly reveal porosity inside the mesocrystals.

The composition of free NPs present at this point determined by EDS matches PbS (Figure S8c,d, Supporting Information) virtually perfectly.

The *third period* is characterized by the change in growth pattern, and the octahedral mesocrystals are transformed into hyperbranched stars representing the most complex superstructure observed in this system. At $t_r = 20$ min, the simultaneous elongation of the six vertexes of the octahedra takes place. It results in six-branched superstructures with a span of $\sim 250-2500$ nm (Figures 5, 7, and S1). For clarity, we shall use from now on the subscripts *meso* and *NP* to denote whether a specific plane of octahedron refers to the mesocrystal or constituent NP, respectively. Each main branch grows along the ⟨100⟩$_{meso}$ direction of the mesocrystal with incipient secondary nanobranches oriented along the four remaining ⟨100⟩$_{meso}$ directions perpendicular to the main branch. By $t_r = 30$ min (Figures 5, 7, and S1), such growth pattern gives the hyperbranched PbS stars described in the beginning. At this point, the packing of NPs within the structures is improved and porosity has decreased compared to the mesocrystals at $t_r = 10$ min (Figure 2a,b). HRTEM images (Figure 3) reveal continuity of the crystal lattices of the superstructure. At this point, some internal reorganization has taken place, probably including both reorganization of NPs and ions/atoms, such as interfacial diffusion and processes analogous to Ostwald ripening.

The *fourth period*, which starts around $t_r = 50$ min and continues until *ca.* $t_r = 5$ h, is characterized by the transformation of the hyperbranched PbS stars into six-arm stars made from faceted rods without particularly sophisticated surface topology (Figures 5 and 7). Secondary NRs of the hyperbranched stars become less defined as a consequence of fusion of several NRs. Tips of microbranches and NRs become flatter. The thickness of the microbranches increases. As a result, at $t_r = 5$ h, six-branched stars made from microrods dominate. Both TEM (Figure 5) and SEM (Figure 7) images indicate that the width of the rods in the new structures matches well the end-to-end distance between nanobranches of the hyperbranched structures.

The disintegration of the six-arm rods into smaller particles occurs during the *fifth period* of the reaction whose onset is approximately associated with $t_r = 5$ h. One can observe multiple broken microbranches (Figures 5 and 7). One can also see multiple points where the branches were broken off—the nicely shaped $100-150$ nm cavities in the ⟨100⟩$_{meso}$ surfaces (arrows in Figure 7). Shorter rods and numerous $\sim 170-500$ nm particles are observed. They cannot be the growth product of original 30 nm NPs. They are the result of the deconstruction of the microrods from the previous period since their diameters and widths match. The number of such particles increases for $t_r = 1-5$ days (Figures 5 and 7), in parallel with the
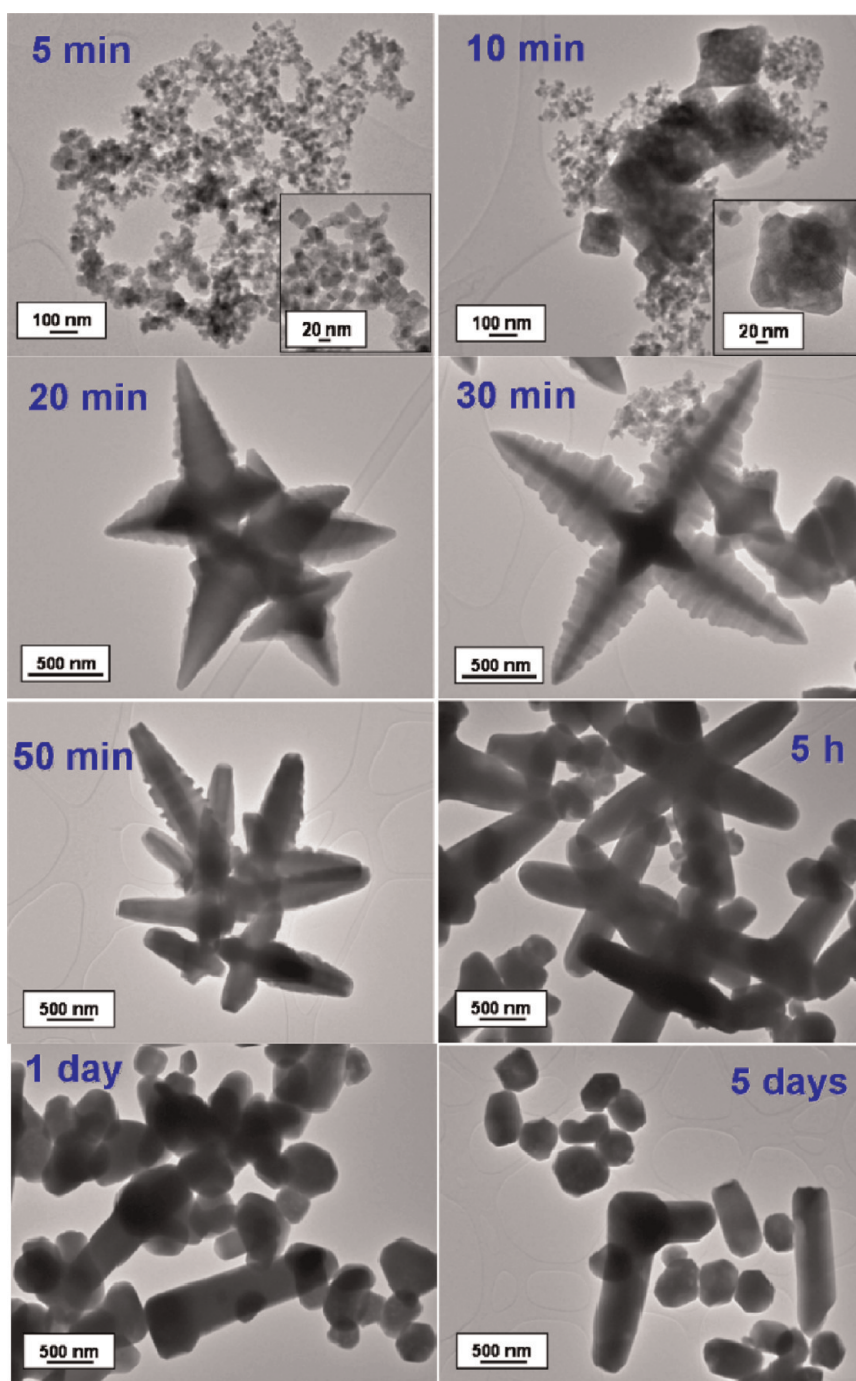
Figure 5. TEM images of the PbS crystals for different reaction times.

decrease of the number of microrods. Inner porosity of the particles at this point is considerably decreased (compare Figure 2 and tomography in Figures S11 and SV12, Supporting Information). This points to important role of ion-exchange-driven recrystallization at this stage. For $t_r = 14$ days, etching of these NPs is observed (Figure S13).

DISCUSSION

The description of the complex geometry of the PbS superstructures and the different stages of their growth raises a number of questions which we shall attempt to answer. Admittedly, some of them generate new questions pertaining to the different forces acting between the NPs and how the geometry of the superstructures reflects such interactions. It is worth noting that the forces responsible for the SA in solution as well as 3D geometry of the superstructures reported here are distinct from those involved in previous reports on evaporation-induced assembly routes[63,64] or CVD.

Why Do PbS NPs Form Hyperbranched Microstructures? Experimental observations of hyperbranched microstructures
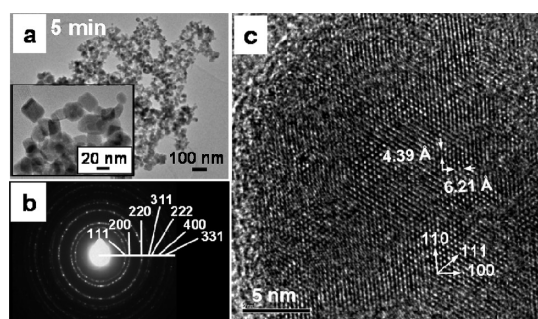
Figure 6. (a) TEM image of PbS NPs obtained at t_r = 5 min. Inset shows TEM image with higher magnification. (b) SAED ring pattern of the group of NPs shown in (a). (c) HRTEM characterization of a PbS nanoparticle.
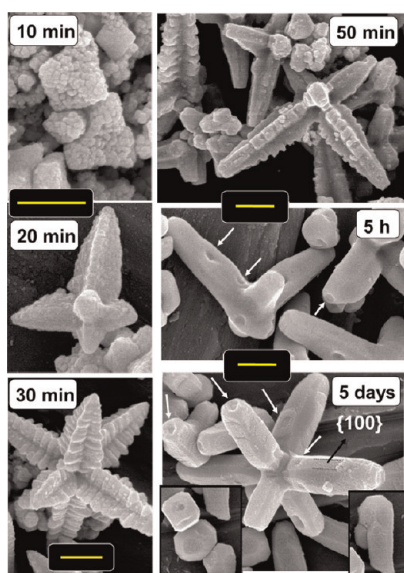

Figure 7. SEM images of the PbS products at different reaction times. All scale bars = 500 nm. Arrows point to the cavities in the {100} crystal faces.

Figure 8. (a) Growth of truncated octahedral seeds containing six {100} and eight {111} crystallographic faces into (first row) cubic and eight-branched crystals and (second row) octahedral and six-branched crystals. (b) Schematics of the nanoparticle assembly leading initially to octahedral mesocrystals (superparticles) and later to hierarchical hyperbranched superstructure.

of PbS are extensive.[23−25,27−39] Despite that, the reasons why they are forming and why the geometry of the superstructures is so peculiar have not been addressed. Surprisingly to us, SA processes have not been considered as a possible formation pathway. Multiple observations of such structures are quite clearly related not to the specific surfactants or solvents but rather to the intrinsic properties of PbS. The hyperbranched stars can be observed with[23,25,28,29,31−36] and without[30] the surfactants whose structure varies quite dramatically and in a variety of different solvents. In our system, DES probably plays the role of the solvent and a polar dynamic capping agent. While reducing the surface energy, it does not prevent the growth of PbS crystallites. Note that branched structures are also observed for other materials crystallizing in dendrites,[65−68] but most of them are random with stochastically determined growth directions and placements of NPs.[69]

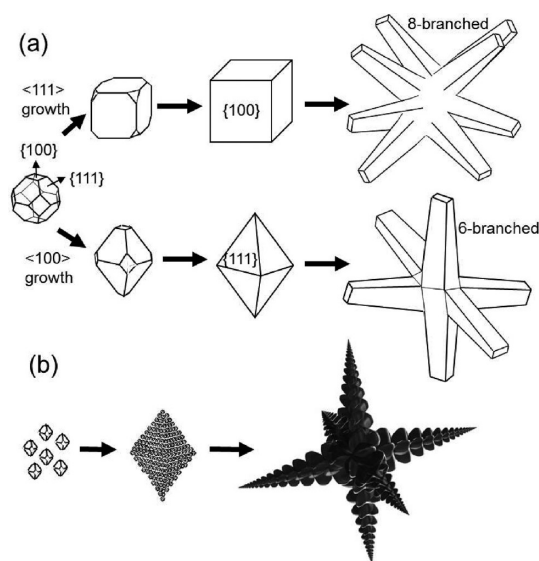To understand the mechanism, we need to start with the growth of nanocrystalline seeds and the

first period in the reaction. It is generally accepted that the difference of relative growth rates of the six {100}$_{NP}$ faces and the eight {111}$_{NP}$ faces[10,20,70] of seeds with a shape of truncated octahedron is responsible for nanoscale geometries[20,24,27,31] (Figure 8a). The faster growth along the eight ⟨111⟩$_{NP}$ directions perpendicular to {111}$_{NP}$ faces results in the elimination of such faces and subsequent formation of {100}$_{NP}$-faceted cubes (Figure 8a). If growth perpendicular to {100}$_{NP}$ faces is preferred, such faces eventually disappear and resulting morphologies are eight-faced octahedra with {111}$_{NP}$ faces. If the latter growth is much faster than that along the ⟨111⟩$_{NP}$ directions and longer growth times are allowed, six-branched star-shaped crystalline NPs are formed due to the growth along the six ⟨100⟩ directions or vertexes of the octahedra (Figure 8a).[10,20] Note these nanoscale stars cannot explain the formation of microscale superstructures, although the geometry does have some similarity. The ⟨100⟩ preferential growth can be favored by the use of cetyltrimethylammonium bromide (CTAB)[25,31,36] and primary amines,[23,28,32−36] as the ones from DES, whose electrostatic interaction with polar {111} faces favors the growth perpendicularly to apolar {100} vertexes.

The second period is characterized by the formation of mesocrystals. They tend to have the octahedral shape. The mesocrystals at t_r ∼ 10 min resemble an enlarged version of NPs. Nevertheless, their appearance cannot be explained via the same growth process as in the first period. SEM images in Figure 7 provide strong evidence that the mesocrystals are formed by association of individual NPs observed in the first

period. Such assemblies are unlikely to be produced in a classical crystallization process with small molecular precursors or ions as the building blocks. The complementary evidence of an assembly pathway can be seen also in the HAADF-STEM images (Figure 2b) and corresponding tomography studies (Figure S8 and video files in Figure SV9, Supporting Information), which show substantial internal porosity with cavities very similar in size to the constituent NPs. These cavities are inevitable when the assembly process involves polydispersed NPs and the match between the neighboring building blocks is deficient. Similar cavities can also be found in the hyperbranched superstructures (Figure 2b and 3D video Figures SV2 and SV3, Supporting Information). These findings are consistent with the notion that NPs can serve as building blocks of microstructures[4,5] and can produce ordered superstructures due to oriented attachment[1−3,7] and potentially other mechanisms,[8−14,70,71] and in particularly with self-limiting association of nanoparticles in supraparticles.[72] The presence of internal pores in relative uniformity in their diameters is consistent with the agglomeration driven by van der Waals attraction being counteracted by electrostatic repulsion.[72]

Identity in the geometrical (octahedral) assembly patterns of NPs and constitutive ions—Pb^{2+} and $S^{2−}$—led to another observation. Formal description of the assembly of mesocrystals and growth of individual NPs from subnanometer scale seeds could potentially be described by the nucleation theory originally developed for atomic precursors in solution.[73,74] The same theory could be equally applicable to the nucleation and growth of mesocrystals with the difference that the "monomers" here are individual NPs. From this perspective, the formation of mesocrystals occurs when the concentration of NPs generated in the first period is well above supersaturation threshold in respect to their agglomeration into mesocrystals.

The *third period* of the reaction leads to the hyperbranched PbS stars. At this point, early NPs are still present in large quantity (Figures 5 and S1). Therefore, they can play the role of building blocks in the transition of the mesocrystals to hyperbranched stars. The clear evidence of that can be seen in HAADF-STEM images (Figure 2a and Figures SV2 and S6, Supporting Information), which show NP attachment to the growing superstructure. The parallelism in the decrease of the amount of NPs in the medium and the concomitant enlargement of the microcrystals (Figures 5 and 7) is consistent with this conclusion, as well. It should be noted that the average size of the NPs at this point, $t_r = 30$ min, is 32.9 nm (±1.1 nm) (Figure S6, Supporting Information), which is identical within the experimental error to the average size of the NPs at $t_r = 5$ min, *i.e.,* 31.3 nm (±10.7 nm) (Figure S7, Supporting Information). This fact indicates minimal Ostwald ripening and, therefore, further asserts secondary

importance of molecular scale precursors and ion exchange in the formation of the superstructures.

A question needs to be raised: why do the NPs form hyperbranched stars and not simply larger mesocrystals continuing the growth pattern of the second period? The switch of the assembly pattern can be understood considering the similarity of mesocrystals to self-limited supraparticles.[72] The switch of the SA pattern happens at the point because the energy of van der Waals attraction can no longer overcome charge−charge electrostatic repulsion between mesocrystals and individual NPs. After this point, weaker forces acting in addition to these two forces, such as dipole−dipole attraction, become pattern-determining interactions. Indeed, geometry of the hyperbranch stars indicates the preferred linear pattern of assembly. The axial anisotropy associated with the presence of electrical dipoles in NPs[10,75−77] is inherent to many nanoscale materials.[78] Previous reports identified the presence of dipole moment in PbS and other NPs with cubic rock-salt structure.[10,20,70] Attraction of NP dipoles has already been implicated in many SA processes.[10,75−77] Moreover, the $\langle100\rangle_{NP}$ axis in PbS and other semiconductor NPs with rock-salt isomorphs such as CdS, CdTe, ZnSe, and PbSe is associated with the greatest dipole.[10] Therefore, the formation of branches along $\langle100\rangle_{meso}$, which is aligned with $\langle100\rangle_{NP}$, is to be expected and is exactly what is observed in the hyperbranched structures (Figure 8b).

It is important to point out that an ensemble of NP dipoles accumulates certain polarization as SA proceeds. The cumulative polarization of the superstructure (or the total dipole moment for head-to-tail arrangement of dipoles) is proportional to the number of NPs assembled. The polarization is directed along the six equivalent $\langle100\rangle_{NP,meso}$ directions represented by the six vertexes. For antiparallel orientation of the dipoles, the dependence would be more sophisticated but still increase with the number of NPs. The polarization increases the energy of the superstructure and, therefore, counteracts the SA process, causing self-limiting. The accumulation of polarization energy can be quite fast. As such, the gradual increase of polarization in the chains of dipolar ZnO NPs assembled in the head-to-tail fashion leads to very short NP chains limited to often 5−10 NPs.[11] This is not true for PbS hyperbranched stars, which are estimated on average to have 6000 to 100 000 NPs. Consequently, there must be some mechanism reducing such polarization and stabilizing the PbS superstructure.

The formation of the stars with the rays practically equal to each other in length is hypothesized to be related to the stabilization of hyperbranched stars. The relief of the polarization build-up polar 1D structures could be attained through the balancing and mutual cancelation of the vectors of accumulating dipoles in opposite directions. For PbS hyperbranched stars,

these directions can be mapped in the simplest case as six vectors all pointing away from the central point of origin resembling the 3D Cartesian system of coordinates. If such cancelation occurs, further assembly will not be prevented by the accumulation of the polarization energy. In general, one can make a parallel with the six ligands/ions positioned equidistantly around a central atom, which is the most popular motif in metal—organic complexes and ionic crystals, respectively. From this perspective, it should not be surprising to find the same motif in nanoscale objects.[10,18,20] Balancing of dipoles in pairs of opposite directions may operate throughout all levels of hierarchy.

Note now that macroscopic cancelation of dipolar vectors pointing to opposite directions is important but does not eliminate a large part of the actual polarization energy. The major components of polarization energy such as strain of the crystal lattice, loss of entropy of polarized molecules of the medium, and distortion of different chemical bonds by electrical field operate over molecular scale distances. As such, a NP of 3.3 nm with a dipole of 42 D, as it is the case for cubic ZnSe,[75] would have the energy of 8.256×10^{-6} eV in a medium with $\varepsilon = 65692.76 \times 10^{-12}$ F·m^{-1} (see detailed calculation in the Supporting Information). Accumulation of dipolar NPs within a microbranch has to imply the redistribution of charges through the growing assembly. For insulating materials and wide band gap semiconductors, for instance, ZnO with conductivity of 205 cm^2·V^{-1}·s^{-1} (bulk),[79] this is impossible. Hence, the NP dipolar chains are short.[11] However, PbS has much higher conductivity of 640 cm^2·V^{-1}·s^{-1} (bulk)[80] than ZnO. The conductivity greatly facilitates the redistribution of charges once the NPs are attached to each other. TEM images in Figure 3, indicating nearly perfect atomic interfaces between the assembled NPs, further support the capability to transport charges over the entire superstructure. The absence of the insulating layer between the individual nanocrystals due to the noncovalent binding of DES is also an important. Finally, the neutralization of the dipolar charges in each arm is never complete, and the dipoles are probably never reduced to zero, which plays a role orienting and assembling new NPs.

Five levels of geometrically self-similar hierarchy can be identified in PbS NP superstructures. Starting from the atomic level of hierarchy, the rock-salt cubic structure of PbS implies that each cation is surrounded by six anions and *vice versa*, forming an octahedron with a characteristic scale of 0.59143 nm (JCPDS 01-078-1054). The next hierarchical level is the truncated octahedral shape of the individual NPs serving as the building blocks of the hyperbranched stars.[10,20,70] As was mentioned, their characteristic scale is *ca.* 30 nm. The following hierarchical level corresponds to the incipient octahedron within each NR, whose typical widths are ~60—150 nm. The octahedral symmetry

among nanobranches and the octahedrons produced by the rays of the PbS stars correspond to the last two levels of self-symmetry with characteristic lengths of 160—500 and ~1500—3000 nm, respectively. The electrostatic balance in dipolar pairs of opposite direction could be ultimately responsible for the all of the octahedral symmetries of the PbS microscale stars throughout the five levels of hierarchy. Obviously, smaller structures and those made by ion-to-ion growth will inevitably display a hierarchical pattern with smaller number of levels although with some similarities related to octahedral geometry.[10,18,20,24,27,31,63]

Why Do the PbS Superstructures Disassemble? If PbS crystals present a certain pattern of polarization, it should be influenced by the dielectric constant of the solvent (Supporting Information),[76] which is evidenced in the last two periods of the reaction (Figure 9).

The next change in assembly pattern occurs at *ca.* $t_r = 50$ min: the NPs remaining in the medium are no longer incorporated along the length of the nano- and microrods, that is, $\langle 100 \rangle_{meso}$ directions, but along the $\langle 111 \rangle_{meso}$ directions. It leads to widening of the rays of the microstars and disappearance of the fine structure of the microbranches. Since this process involves breaking the octahedral symmetry among the NRs, it should be less favorable than the previous SA along $\langle 100 \rangle_{meso}$ directions and alignment of dipoles.[8,10,11] This is reflected by the slower rate of the process with $t_r = \sim 50$ min—5 h as compared to SA along the $\langle 100 \rangle_{meso}$ direction, which has $t_r = 30$ min.

Similarly to the previous periods, the attachment of NPs in this period occurs mostly epitaxially (Figure 10b). However, in some cases, in HRTEM images (Figure 10c—e), we also see non-epitaxial interfaces between the microrods and NPs. This suggests that the elementary building blocks in the *fourth period* are not ions but NPs as well as in the previous ones. However, the final generation of much smoother surfaces is due to the complementary contribution of ionic diffusion accelerated in this period. Analysis of the images reveals a [0—11] projection of the PbS crystal within the microrod, while all of the NPs on the surface correspond to [001] axis of PbS. Thus, both PbS lattices share the $\langle 011 \rangle_{NP}$ direction and are tilted 45° with respect to each other. Moiré patterns characteristic of the two crystals slightly overlaid at a small angle are detected. These observations might indicate that the incorporation of the NPs into the microstructures involves non-epitaxial attachment by sharing the $\langle 110 \rangle_{NP}$ common direction potentially followed by epitaxial reorganization. Such NP reorientation is analogous to atomic-level rearrangements previously observed in NPs under the electron beam[81] and reorientation/recrystallization of CdTe NPs assembled in chains to produce nanowires.[8] It also does not rule out additional contribution of ionic diffusion.
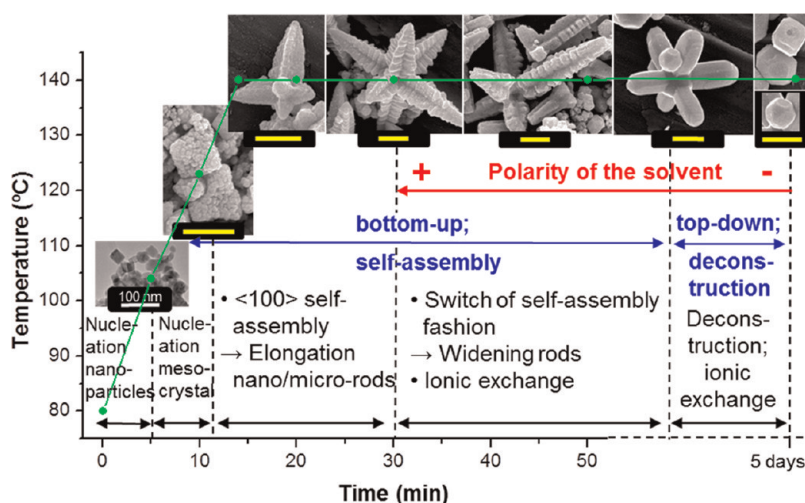
Figure 9. Temperature profile of reaction mixture (green line). TEM or SEM images of the PbS products at different reaction times. Scale bars are 500 nm except for the image at t_r = 5 min.
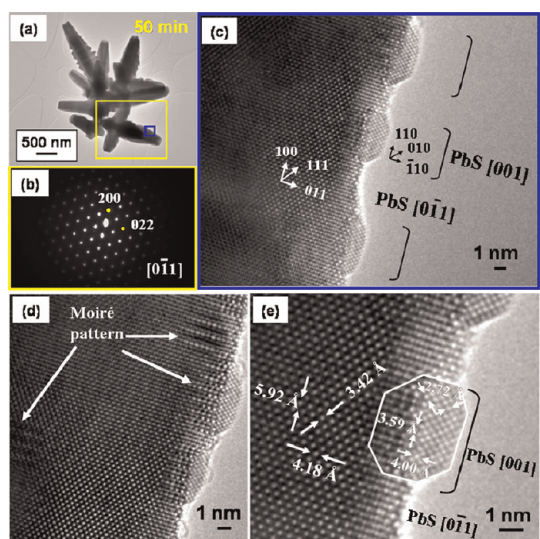

Figure 10. Characterization of the PbS particles obtained at t_r = 50 min. (a) TEM image. (b) SAED pattern along the [0−11] zone axis of the particle highlighted in (a). (c) HRTEM image of an area within the highlighted part in (a). (d,e) HRTEM images indicating Moiré patterns and the atomic interplanar distances.

Figure 11. Characterization of PbS products obtained at t_r = 5 h (first column) and t_r = 5 days (second column). (a) TEM image of rods and particles at t_r = 5 h. Arrows point to thinner tips of the rods. (b) Fourier transform pattern of the (c) HRTEM image corresponding to the area squared in (a). (d) TEM image of a particle undergoing deconstruction at t_r = 5 days. (e) SAED pattern of the particle shown in (d) along the [0−11] zone axis. (f) HRTEM image of the area squared in (d).

The reason for the switch of the SA pattern at this stage is the change of electrical properties of the medium. It is known that urea/choline chloride DES is unstable upon heating (see detailed discussion in Supporting Information, Figures S14 and S15 and Table S1).[54] The ^{1}H NMR spectra (Figure S14, Supporting Information) of the reaction medium evidence that urea decomposition becomes noticeable at $t_d >$ 30 min. It corresponds very well to the transition from the third to the fourth period. Dielectric spectroscopy measurements of the [DES/water] mixture at different reaction times (Figure S16, Supporting Information) showed that during the initial stage between t_d = 0 and 10 min the permittivity increases, which is ascribed to the initial evaporation of water. From t_d = 10−30 min,
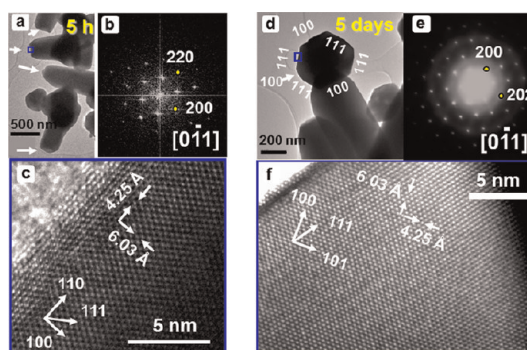
the permittivity is kept constant and corresponds to a medium which undergoes negligible changes, as confirmed by ^{1}H NMR. However, between t_d = 30 min and t_d = 24 h, there is a noticeable gradual decrease of both the real and imaginary parts of the permittivity, which can be related to a decrease of polarity over the entire range of frequencies.

Reduction of dielectric constants results in the increase of both electrostatic repulsion and attraction similarly to what had been observed before by direct variation of the mixed solvent.[82] In this system, charge−charge repulsion overcomes dipolar, van der Waals, and other attraction interactions[82] due to longer effective range. This leads to the disassembly/deconstruction of the SA structures. Note that decomposition of DES will also change its ability to cap/stabilize PbS NPs. This may also contribute to change the charge state and orientation of dipole moment.[76,82] Besides retaining its orientation along the $\langle 100 \rangle_{NP}$ axes, a dipole

can flip its direction along the $\langle 110 \rangle_{NP}$ and $\langle 111 \rangle_{NP}$ directions or cease to exist at all.[10]

Extensive deconstruction is characteristic for the *fifth period* of the reaction. Besides simple mechanical breakage of the microscale structures,[28,33,34] cavities or holes are formed on the $\{100\}_{meso}$ faces (Figure 7). The formation of such cavities is characteristic for PbS[16,23,26,29,30,35−38] and can be attributed to the points where the branches break off. Both stress and accumulation of charges at these points are the greatest. Concomitantly, four new $\{111\}_{meso}$ faces are developed at the expense of disappearance of $\{100\}_{meso}$ faces (Figure 11). Finally, the complete erosion of the rods through the cavities in combination with further reconstruction process leads to their rupture into faceted particles several hundred nanometers in size (Figures 5, 7, and 11a,d). SAED pattern (Figure 11e) and HRTEM image (Figure 11f) verify the monocrystalline nature of these particles and continuous crystal lattice. This also indicates that the Ostwald ripening and ion-related growth process play a substantial role at this stage.

The geometry of these remnant particles is the derivative of various types of tetradecahedrons and cuboctahedrons, confirming the development of $\{111\}_{NP}$ faces at the cost of reduction of $\{100\}_{NP}$ surface area (SEM in Figure 7; TEM of truncated octahedral shape oriented along $[110]^{70}$ in Figure 11d; HAADF-STEM images, 3D reconstruction and proposed models for the particles in Figure 2c,d and Supporting Information Figure S11; video from the 3D reconstruction of the particles in Supporting Information Figure SV12). One should also note that some of the resulting NPs at the end of the deconstruction possess the same type of morphology, that is, truncated octahedron with both $\{100\}_{NP}$ and $\{111\}_{NP}$ faces, although with a different size than the assigned one to the PbS seeds nucleated in the first period, assessing the thermodynamic stability of a ubiquitous octahedral pattern.

The processes typical for the fifth period are analogous to the previously reported disassembly/deconstruction in chains of ZnO NPs,[11] as well as the decrease CdTe NPs[82] chain lengths upon decrease of the polarity of the medium. Decrease of the polarity of the medium (Figure S16) increases repulsive forces within microbranches. The octahedral arrangements of microbranches are not stable under these circumstances. Note, however, that the deconstruction process here involves apparently greater forces leading to the break-off of a continuous microcrystal rather than the previous disassembly/nonassembly of discrete NPs. Also note that the activation energy for the breakage of the crystal lattice and conversion of anisotropic nano/submicrometer structures to more energy-efficient isotropic organization might be dependent on the reorganization energy of ions on NP interfaces by surface diffusion, which is quite low for PbS[83,84] because similar deconstruction of PbS rods was observed under the electron beam.[85]

CONCLUSIONS

The major thrust of this study was to gain better understanding of the mechanisms behind the SA (and deconstruction) of PbS crystals leading to complex geometries. It was conclusively shown that SA processes are responsible for the growth of PbS superstructures. The complexity of their geometry is related to several switches in SA patterns. Assemblies in mesocrystals (also known as supraparticles) are governed by the balance between van der Waals attraction and electrostatic repulsion. A parallel can be drawn between the process of NP SA into mesocrystals and nucleation of individual NPs being driven by oversaturation of NPs and few-atom intermediates.

Assembly into the hyperbranched superstructures is driven by dipolar attraction counterbalanced by a variety of repulsive electrostatic forces. The critical role of polarization energy as a self-limiting factor for SA is highlighted. Unlike many other systems, PbS superstructures with octahedral symmetries are able to minimize its accumulation, partially because of the balance of dipolar branches in pairs of opposite direction. Also, its high conductivity and the absence of the insulating gaps between the NPs makes possible the extended assembly by facilitating charge transfer and polarization reduction. Decrease of polarity of the medium results in the deconstruction of the superstructure because of the increase of repulsive interactions. Using this knowledge, one can realize controlled PbS self-assembly in a format suitable for (opto)electronic applications.

EXPERIMENTAL SECTION

Lead(IV) acetate (95%, Sigma), thioacetamide (99%, ACS reagent), urea (ultra, Sigma), and choline chloride ($\geq 97\%$, Fluka) were used as received. DES was prepared by mixing the components urea and choline chloride in the molar ratio 2:1, as corresponds to the eutectic point, and heating to 80 °C in a furnace until a homogeneous, viscous liquid was formed.[53] The synthesis was performed as follows. Deionized water (6 mL) was added to DES (30 mL at 37 °C, 35.70 g) under stirring in a round-bottom flask of 100 mL. After heating to 80 °C under stirring, 12 mL of the solvent was used to dissolve the thioacetamide (12 mmol, 0.9134 g) and the rest of the liquid was employed as a solvent for the lead(IV) acetate (12 mmol, 5.3206 g). Both precursor solutions were kept under stirring in an oil bath at 80 °C until transparent. Upon hot injection at 80 °C of the colorless thioacetamide solution into the yellowish lead(IV) acetate, the mixture turned opaque, dark brown. Then the flask was connected to a condenser, and the temperature was increased to 140 °C in 14 min. The solution turned black quickly (<5 min) after the hot injection. Aliquots from the same batch were collected at different reaction times. After cooling, the resulting products were purified by dissolution in water

followed by dialysis, centrifugation, and drying in a furnace at temperature ≤80 °C.

Selected area electron diffraction (SAED) and transmission electron microscopy (TEM) at both low- and high-resolution (HRTEM) modes were performed in JEOL 3011 and JEOL 3000 FEG microscopes. Tomography experiments based on high-angle annular dark-field (HAADF) imaging in the scanning transmission electron microscopy (STEM) mode were performed on a JEOL 2010F electron microscope tilting the sample about a single axis using a Fischione ultra-narrow gap tomography holder. Tilt series were aligned and reconstructed using Inspect3D. Chemical composition of the crystals was determined by energy-dispersive X-ray analysis (EDS). Scanning electron microscopy (SEM) was performed on a JSM-6330F FEG microscope working at 20 kV. X-ray diffraction (XRD) of the powders was carried out using a Rigaku rotating anode X-ray diffractometer with Cu Kα radiation (λ = 1.5418 Å).

Chemical decomposition of the DES/water solvent was evaluated by means of dielectric spectroscopy and ^{1}H NMR. Dielectric spectroscopy measurements were carried out using a broad-band dielectric spectrometer (Novocontrol Technologies GmbH) in the frequency range from 1 Hz to 4 MHz. In order to avoid the time-dependent fluctuations typical of the measurements performed at 25 °C, the samples were cooled (in *ca.* 30 min) to −70 °C. The multiple measurements done at that temperature coincided well. ^{1}H NMR spectra (500 MHz) were recorded using a Bruker spectrometer DRX-500, placing the nondiluted samples in capillary tubes and using chloroform ($CHCl_3$) as external reference.

Conflict of Interest: The authors declare no competing financial interest.

Supporting Information Available: NPs size histogram, TEM, HRTEM, SEM, HAADF-STEM-based electron tomography, XRD, dielectric spectroscopy, UV−vis absorbance, UV−vis emission, and ^{1}H NMR spectra and discussion. Urea decomposition reactions. Calculation of the electric potential energy of a dipolar nanoparticle. Analysis of the influence of experimental variables in the resulting products. This material is available free of charge *via* the Internet at http://pubs.acs.org.

REFERENCES AND NOTES

1. Grzybowski, B. A.; Wilmer, C. E.; Kim, J.; Browne, K. P.; Bishop, K. J. M. Self-Assembly: From Crystals to Cells. *Soft Matter.* **2009**, *5*, 1110–1128.

2. Nie, Z.; Petukhova, A.; Kumacheva, E. Properties and Emerging Applications of Self-Assembled Structures Made from Inorganic Nanoparticles. *Nat. Nanotechnol.* **2010**, *5*, 15–25.

3. Choi, C. L.; Alivisatos, A. P. From Artificial Atoms to Nanocrystal Molecules: Preparation and Properties of More Complex Nanostructures. *Annu. Rev. Phys. Chem.* **2010**, *61*, 369–389.

4. Cölfen, H.; Antonietti, M. Mesocrystals: Inorganic Superstructures Made by Highly Parallel Crystallization and Controlled Alignment. *Angew. Chem., Int. Ed.* **2005**, *44*, 5576–5591.

5. Song, R. Q.; Cölfen, H. Mesocrystals - Ordered Nanoparticle Superstructures. *Adv. Mater.* **2010**, *22*, 1301–1330.

6. Daniel, M. C.; Astruc, D. Gold Nanoparticles: Assembly, Supramolecular Chemistry, Quantum-Size-Related Properties, and Applications toward Biology, Catalysis, and Nanotechnology. *Chem. Rev.* **2004**, *104*, 293–346.

7. Shevchenko, E. V.; Talapin, D. V.; Kotov, N. A.; O'Brien, S.; Murray, C. B. Structural Diversity in Binary Nanoparticle Superlattices. *Nature* **2006**, *439*, 55–59.

8. Tang, Z.; Kotov, N. A.; Giersig, M. Spontaneous Organization of Single CdTe Nanoparticles into Luminescent Nanowires. *Science* **2002**, *297*, 237–240.

9. O'Sullivan, C.; Gunning, R. D.; Sanyal, A.; Barrett, C. A.; Geaney, H.; Laffir, F. R.; Ahmed, S.; Ryan, K. M. Spontaneous Room Temperature Elongation of CdS and Ag_2S Nanorods *via* Oriented Attachment. *J. Am. Chem. Soc.* **2009**, *131*, 12250–12257.

10. Cho, K. S.; Talapin, D. V.; Gaschler, W.; Murray, C. B. Designing PbSe Nanowires and Nanorings through Oriented Attachment of Nanoparticles. *J. Am. Chem. Soc.* **2005**, *127*, 7140–7147.

11. Yang, M.; Sun, K.; Kotov, N. A. Formation and Assembly-Disassembly Processes of ZnO Hexagonal Pyramids Driven by Dipolar and Excluded Volume Interactions. *J. Am. Chem. Soc.* **2010**, *132*, 1860–1872.

12. Tang, Z.; Wang, Y.; Shanbhag, S.; Giersig, M.; Kotov, N. A. Spontaneous Transformation of CdTe Nanoparticles into Angled Te Nanocrystals: From Particles and Rods to Checkmarks, X-Marks, and Other Unusual Shapes. *J. Am. Chem. Soc.* **2006**, *128*, 6730–6736.

13. Tang, Z.; Zhang, Z.; Wang, Y.; Glotzer, S. C.; Kotov, N. A. Self-Assembly of CdTe Nanocrystals into Free-Floating Sheets. *Science* **2006**, *314*, 274–278.

14. Srivastava, S.; Santos, A.; Critchley, K.; Kim, K. S.; Podsiadlo, P.; Sun, K.; Lee, J.; Xu, C.; Lilly, G. D.; Glotzer, S. C.; Kotov, N. A. Light-Controlled Self-Assembly of Semiconductor Nanoparticles into Twisted Ribbons. *Science* **2010**, *327*, 1355–1359.

15. Simon, P.; Zahn, D.; Lichte, H.; Kniep, R. Intrinsic Electric Dipole Fields and the Induction of Hierarchical Form Developments in Fluorapatite-Gelatine Nanocomposites: A General Principle for Morphogenesis of Biominerals? *Angew. Chem., Int. Ed.* **2006**, *45*, 1911–1915.

16. Wise, F. W. Lead Salt Quantum Dots: The Limit of Strong Quantum Confinement. *Acc. Chem. Res.* **2000**, *33*, 773–780.

17. Bakueva, L.; Gorelikov, I.; Musikhin, S.; Zhao, X. S.; Sargent, E. H.; Kumacheva, E. PbS Quantum Dots with Stable Efficient Luminescence in the Near-IR Spectral Range. *Adv. Mater.* **2004**, *16*, 926–929.

18. Scheele, M.; Oeschler, N.; Veremchuk, I.; Peters, S.-O.; Littig, A.; Kornowski, A.; Klinke, C.; Weller, H. Thermoelectric Properties of Lead Chalcogenide Core−Shell Nanostructures. *ACS Nano* **2011**, *5*, 8541–8551.

19. Dresselhaus, M. S.; Chen, G.; Tang, M. Y.; Yang, R.; Lee, H.; Wang, D.; Ren, Z.; Fleurial, J. P.; Gogna, P. New Directions for Low-Dimensional Thermoelectric Materials. *Adv. Mater.* **2007**, *19*, 1043–1053.

20. Lee, S. M.; Jun, Y. W.; Cho, S. N.; Cheon, J. Single-Crystalline Star-Shaped Nanocrystals and Their Evolution: Programming the Geometry of Nano-Building Blocks. *J. Am. Chem. Soc.* **2002**, *124*, 11244–11245.

21. Yu, D.; Wang, D.; Meng, Z.; Lu, J.; Qian, Y. Synthesis of Closed PbS Nanowires with Regular Geometric Morphologies. *J. Mater. Chem.* **2002**, *12*, 403–405.

22. Wang, Z.; Schliehe, C.; Wang, T.; Nagaoka, Y.; Cao, Y. C.; Bassett, W. A.; Wu, H.; Fan, H.; Weller, H. Deviatoric Stress Driven Formation of Large Single-Crystal PbS Nanosheet from Nanoparticles and *In Situ* Monitoring of Oriented Attachment. *J. Am. Chem. Soc.* **2011**, *133*, 14484–14487.

23. Zhang, W.; Yang, Q.; Xu, L.; Yu, W.; Qian, Y. Growth of PbS Crystals from Nanocubes to Eight-Horn-Shaped Dendrites through a Complex Synthetic Route. *Mater. Lett.* **2005**, *59*, 3383–3388.

24. Zhao, N.; Qi, L. Low-Temperature Synthesis of Star-Shaped PbS Nanocrystals in Aqueous Solutions of Mixed Cationic/Anionic Surfactants. *Adv. Mater.* **2006**, *18*, 359–362.

25. Wang, N.; Cao, X.; Guo, L.; Yang, S.; Wu, Z. Facile Synthesis of PbS Truncated Octahedron Crystals with High Symmetry and their Large-Scale Assembly into Regular Patterns by a Simple Solution Route. *ACS Nano* **2008**, *2*, 184–190.

26. Zhang, X. H.; Jia, C.; Chen, Y. Q.; Su, Y.; Zhou, H. Y. A Mixed Solvothermal Route to Synthesis of Dice-like PbS. *J. Chin. Chem. Soc.* **2008**, *55*, 1221–1224.

27. Zhao, Z.; Zhang, K.; Zhang, J.; Yang, K.; He, C.; Dong, F.; Yang, B. Synthesis of Size and Shape Controlled PbS Nanocrystals and Their Self-Assembly. *Colloids Surf., A* **2010**, *355*, 114–120.

28. Wang, D.; Yu, D.; Shao, M.; Liu, X.; Yu, W.; Qian, Y. Dendritic Growth of PbS Crystals with Different Morphologies. *J. Cryst. Growth* **2003**, *257*, 384–389.

29. Ma, Y.; Qi, L.; Ma, J.; Cheng, H. Hierarchical, Star-Shaped PbS Crystals Formed by a Simple Solution Route. *Cryst. Growth Des.* **2004**, *4*, 351–354.

30. Ni, Y.; Liu, H.; Wang, F.; Liang, Y.; Hong, J.; Ma, X.; Xu, Z. Shape Controllable Preparation of PbS Crystals by a Simple Aqueous Phase Route. *Cryst. Growth Des.* **2004**, *4*, 759–764.

31. Zhou, G.; Lü, M.; Xiu, Z.; Wang, S.; Zhang, H.; Zhou, Y.; Wang, S. Controlled Synthesis of High-Quality PbS Star-Shaped Dendrites, Multipods, Truncated Nanocubes, and Nanocubes and Their Shape Evolution Process. *J. Phys. Chem. B* **2006**, *110*, 6543–6548.

32. Bakshi, M. S.; Thakur, P.; Sachar, S.; Kaur, G.; Banipal, T. S.; Possmayer, F.; Petersen, N. O. Aqueous Phase Surfactant Selective Shape Controlled Synthesis of Lead Sulfide Nanocrystals. *J. Phys. Chem. C* **2007**, *111*, 18087–18098.

33. Shao, S.; Zhang, G.; Zhou, H.; Sun, P.; Yuan, Z.; Li, B.; Ding, D.; Chen, T. Morphological Evolution of PbS Crystals under the Control of L-Lysine at Different pH Values: The Ionization Effect of the Amino Acid. *Solid State Sci.* **2007**, *9*, 725–731.

34. Xiang, J.; Cao, H.; Wu, Q.; Zhang, S.; Zhang, X. L-Cysteine-Assisted Self-Assembly of Complex PbS Structures. *Cryst. Growth Des.* **2008**, *8*, 3935–3940.

35. Zhu, J.; Duan, W.; Sheng, Y. Uniform PbS Hopper (Skeletal) Crystals Grown by a Solution Approach. *J. Cryst. Growth* **2009**, *311*, 355–357.

36. Ding, B.; Shi, M.; Chen, F.; Zhou, R.; Deng, M.; Wang, M.; Chen, H. Shape-Controlled Synthesis of PbS Submicro-/Nano-Crystals *via* Hydrothermal Method. *J. Cryst. Growth* **2009**, *311*, 1533–1538.

37. Zhao, P.; Wang, J.; Cheng, G.; Huang, K. Fabrication of Symmetric Hierarchical Hollow PbS Microcrystals *via* a Facile Solvothermal Process. *J. Phys. Chem. B* **2006**, *110*, 22400–22406.

38. Wang, A.-J.; Liao, Q.-C.; Feng, J.-J.; Zhang, P.-P.; Zhang, Z.-M.; Chen, J.-R. D-Penicillamine-Assisted Self-Assembly of Hierarchical PbS Microstars with Octa-Symmetric-Dendritic Arms. *Cryst. Growth Des.* **2012**, *12*, 832–841.

39. Zuo, F.; Yan, S.; Zhang, B.; Zhao, Y.; Xie, Y. L-Cysteine-Assisted Synthesis of PbS Nanocube-Based Pagoda-like Hierarchical Architectures. *J. Phys. Chem. C* **2008**, *112*, 2831–2835.

40. Lau, Y. K. A.; Chernak, D. J.; Bierman, M. J.; Jin, S. Formation of PbS Nanowire Pine Trees Driven by Screw Dislocations. *J. Am. Chem. Soc.* **2009**, *131*, 16461–16471.

41. Ge, J. P.; Wang, J.; Zhang, H. X.; Wang, X.; Peng, Q.; Li, Y. D. Orthogonal PbS Nanowire Arrays and Networks and Their Raman Scattering Behavior. *Chem.—Eur. J.* **2005**, *11*, 1889–1894.

42. Nichols, P. L.; Sun, M.; Ning, C. Z. Influence of Supersaturation and Spontaneous Catalyst Formation on the Growth of PbS Wires: Toward a Unified Understanding of Growth Modes. *ACS Nano* **2011**, *5*, 8730–8738.

43. Wang, L.; Xu, L.; Kuang, H.; Xu, C.; Kotov, N. Dynamic Nanoparticles Assemblies. *Acc. Chem. Res.* **2012**, 10.1021/ar200305f.

44. Luque, A.; Martí, A.; Nozik, A. J. Solar Cells Based on Quantum Dots: Multiple Exciton Generation and Intermediate Bands. *MRS Bull.* **2007**, *32*, 236–241.

45. Schaller, R. D.; Sykora, M.; Pietryga, J. M.; Klimov, V. I. Seven Excitons at a Cost of One: Redefining the Limits for Conversion Efficiency of Photons into Charge Carriers. *Nano Lett.* **2006**, *6*, 424–429.

46. Pijpers, J. J. H.; Ulbricht, R.; Tielrooij, K. J.; Osherov, A.; Golan, Y.; Delerue, C.; Allan, G.; Bonn, M. Assessment of Carrier-Multiplication Efficiency in Bulk PbSe and PbS. *Nat. Phys.* **2009**, *5*, 811–814.

47. Beard, M. C.; Midgett, A. G.; Hanna, M. C.; Luther, J. M.; Hughes, B. K.; Nozik, A. J. Comparing Multiple Exciton Generation in Quantum Dots To Impact Ionization in Bulk Semiconductors: Implications for Enhancement of Solar Energy Conversion. *Nano Lett.* **2010**, *10*, 3019–3027.

48. Thielsch, R.; Böhme, T.; Reiche, R.; Schläfer, D.; Bauer, H. D.; Böttcher, H. Quantum-Size Effects of PbS Nanocrystallites in Evaporated Composite Films. *Nanostruct. Mater.* **1998**, *10*, 131–149.

49. Law, M.; Greene, L. E.; Johnson, J. C.; Saykally, R.; Yang, P. Nanowire Dye-Sensitized Solar Cells. *Nat. Mater.* **2005**, *4*, 455–459.

50. Gur, I.; Fromer, N. A.; Chen, C. P.; Kanaras, A. G.; Alivisatos, A. P. Hybrid Solar Cells with Prescribed Nanoscale Morphologies Based on Hyperbranched Semiconductor Nanocrystals. *Nano Lett.* **2007**, *7*, 409–414.

51. Greenham, N. C.; Peng, X.; Alivisatos, A. P. Charge Separation and Transport in Conjugated-Polymer/Semiconductor-Nanocrystal Composites Studied by Photoluminescence Quenching and Photoconductivity. *Phys. Rev. B* **1996**, *54*, 17628–17637.

52. Zhang, S.; Cyr, P. W.; McDonald, S. A.; Konstantatos, G.; Sargent, E. H. Enhanced Infrared Photovoltaic Efficiency in PbS Nanocrystal/Semiconducting Polymer Composites: 600-Fold Increase in Maximum Power Output *via* Control of the Ligand Barrier. *Appl. Phys. Lett.* **2005**, *87*, 1–3.

53. Abbott, A. P.; Capper, G.; Davies, D. L.; Rasheed, R. K.; Tambyrajah, V. Novel Solvent Properties of Choline Chloride/Urea Mixtures. *Chem. Commun.* **2003**, *9*, 70–71.

54. Morris, R. E. Ionothermal Synthesis - Ionic Liquids as Functional Solvents in the Preparation of Crystalline Materials. *Chem. Commun.* **2009**, 2990–2998.

55. Cooper, E. R.; Andrews, C. D.; Wheatley, P. S.; Webb, P. B.; Wormald, P.; Morris, R. E. Ionic Liquids and Eutectic Mixtures as Solvent and Template in Synthesis of Zeolite Analogues. *Nature* **2004**, *430*, 1012–1016.

56. Antonietti, M.; Kuang, D.; Smarsly, B.; Zhou, Y. Ionic Liquids for the Convenient Synthesis of Functional Nanoparticles and Other Inorganic Nanostructures. *Angew. Chem., Int. Ed.* **2004**, *43*, 4988–4992.

57. Zhang, J.; Wu, T.; Chen, S.; Feng, P.; Bu, X. Versatile Structure-Directing Roles of Deep-Eutectic Solvents and Their Implication in the Generation of Porosity and Open Metal Sites for Gas Storage. *Angew. Chem., Int. Ed.* **2009**, *48*, 3486–3490.

58. Liao, H. G.; Jiang, Y. X.; Zhou, Z. Y.; Chen, S. P.; Sun, S. G. Shape-Controlled Synthesis of Gold Nanoparticles in Deep Eutectic Solvents for Studies of Structure-Functionality Relationships in Electrocatalysis. *Angew. Chem., Int. Ed.* **2008**, *47*, 9100–9103.

59. Guloy, A. M.; Ramlau, R.; Tang, Z.; Schnelle, W.; Baitinger, M.; Grin, Y. A Guest-Free Germanium Clathrate. *Nature* **2006**, *443*, 320–323.

60. Machol, J. L.; Wise, F. W.; Patel, R. C.; Tanner, D. B. Vibronic Quantum Beats in PbS Microcrystallites. *Phys. Rev. B* **1993**, *48*, 2819–2822.

61. Santoni, A.; Paolucci, G.; Santoro, G.; Prince, K. C.; Christensen, N. E. Band Structure of Lead Sulphide. *J. Phys.: Condens. Matter* **1992**, *4*, 6759–6768.

62. Critchley, K.; Khanal, B. P.; Górzny, M. L.; Vigderman, L.; Evans, S. D.; Zubarev, E. R.; Kotov, N. A. Near-Bulk Conductivity of Gold Nanowires as Nanoscale Interconnects and the Role of Atomically Smooth Interface. *Adv. Mater.* **2010**, *22*, 2338–2342.

63. Miszta, K.; de Graaf, J.; Bertoni, G.; Dorfs, D.; Brescia, R.; Marras, S.; Ceseracciu, L.; Cingolani, R.; van Roij, R.; Dijkstra, M.; Manna, L. Hierarchical Self-Assembly of Suspended

Branched Colloidal Nanocrystals into Superlattice Structures. *Nat. Mater.* **2011**, *10*, 872–876.

64. Huang, T.; Zhao, Q.; Xiao, J.; Qi, L. Controllable Self-Assembly of PbS Nanostars into Ordered Structures: Close-Packed Arrays and Patterned Arrays. *ACS Nano* **2010**, *4*, 4707–4716.

65. Thongtem, T.; Jaroenchaichana, J.; Thongtem, S. Cyclic Microwave-Assisted Synthesis of Flower-like and Hexapod Silver Bismuth Sulfide. *Mater. Lett.* **2009**, *63*, 2163–2166.

66. Polshettiwar, V.; Baruwati, B.; Varma, R. S. Self-Assembly of Metal Oxides into Three-Dimensional Nanostructures: Synthesis and Application in Catalysis. *ACS Nano* **2009**, *3*, 728–736.

67. Cao, M.; Liu, T.; Gao, S.; Sun, G.; Wu, X.; Hu, C.; Zhong, L. W. Single-Crystal Dendritic Micro-pines of Magnetic α-Fe$_2$O$_3$: Large-Scale Synthesis, Formation Mechanism, and Properties. *Angew. Chem., Int. Ed.* **2005**, *44*, 4197–4201.

68. Hu, M.; Jiang, J. S.; Li, X. D. Surfactant-Assisted Hydrothermal Synthesis of Dendritic Magnetite Microcrystals. *Cryst. Growth Des.* **2009**, *9*, 820–824.

69. Ben-Jacob, E.; Garik, P. The Formation of Patterns in Nonequilibrium Growth. *Nature* **1990**, *343*, 523–530.

70. Wang, Z. L. Transmission Electron Microscopy of Shape-Controlled Nanocrystals and Their Assemblies. *J. Phys. Chem. B* **2000**, *104*, 1153–1175.

71. Jun, Y. W.; Lee, J. H.; Choi, J. S.; Cheon, J. Symmetry-Controlled Colloidal Nanocrystals: Nonhydrolytic Chemical Synthesis and Shape Determining Parameters. *J. Phys. Chem. B* **2005**, *109*, 14795–14806.

72. Xia, Y.; Nguyen, T. D.; Yang, M.; Lee, B.; Santos, A.; Podsiadlo, P.; Tang, Z.; Glotzer, S. C.; Kotov, N. A. Self-Assembly of Self-Limiting Monodisperse Supraparticles from Polydisperse Nanoparticles. *Nat. Nanotechnol.* **2011**, *6*, 580–587.

73. Lamer, V. K.; Dinegar, R. H. Theory, Production and Mechanism of Formation of Monodispersed Hydrosols. *J. Am. Chem. Soc.* **1950**, *72*, 4847–4854.

74. Park, J.; Joo, J.; Soon, G. K.; Jang, Y.; Hyeon, T. Synthesis of Monodisperse Spherical Nanocrystals. *Angew. Chem., Int. Ed.* **2007**, *46*, 4630–4660.

75. Shim, M.; Guyot-Sionnest, P. Permanent Dipole Moment and Charges in Colloidal Semiconductor Quantum Dots. *J. Chem. Phys.* **1999**, *111*, 6955–6964.

76. Shanbhag, S.; Kotov, N. A. On the Origin of a Permanent Dipole Moment in Nanocrystals with a Cubic Crystal Lattice: Effects of Truncation, Stabilizers, and Medium for CdS Tetrahedral Homologues. *J. Phys. Chem. B* **2006**, *110*, 12211–12217.

77. Sinyagin, A.; Belov, A.; Kotov, N. Monte Carlo Simulation of Linear Aggregate Formation from CdTe Nanoparticles. *Modell. Simul. Mater. Sci. Eng.* **2005**, *13*, 389–399.

78. Blanton, S. A.; Leheny, R. L.; Hines, M. A.; Guyot-Sionnest, P. Dielectric Dispersion Measurements of CdSe Nanocrystal Colloids: Observation of a Permanent Dipole Moment. *Phys. Rev. Lett.* **1997**, *79*, 865–868.

79. Look, D. C.; Reynolds, D. C.; Sizelove, J. R.; Jones, R. L.; Litton, C. W.; Cantwell, G.; Harsch, W. C. Electrical Properties of Bulk ZnO. *Solid State Commun.* **1998**, *105*, 399–401.

80. Putley, E. H. Electrical Conductivity in the Compounds PbS, PbSe, PbTe. *Proc. Phys. Soc. London, Sect. B* **1952**, *65*, 388–389.

81. Smith, D. J.; Petford-Long, A. K.; Wallenberg, L. R.; Bovin, J. O. Dynamic Atomic-Level Rearrangements in Small Gold Particles. *Science* **1986**, *233*, 872–875.

82. Lilly, G. D.; Lee, J.; Sun, K.; Tang, Z.; Kim, K. S.; Kotov, N. A. Media Effect on CdTe Nanowire Growth: Mechanism of Self-Assembly, Ostwald Ripening, and Control of NW Geometry. *J. Phys. Chem. C* **2008**, *112*, 370–377.

83. Watson, E. B.; Cherniak, D. J.; Frank, E. A. Retention of Biosignatures and Mass-Independent Fractionations in Pyrite: Self-Diffusion of Sulfur. *Geochim. Cosmochim. Acta* **2009**, *73*, 4792–4802.

84. Seltzer, M. S.; Wagner, J. B. Diffusion of Lead in Lead Sulphide at 700 Degrees C. *J. Phys. Chem. Solids* **1963**, *24*, 1525–1530.

85. Warner, J. H. Self-Assembly of Ligand-Free PbS Nanocrystals into Nanorods and Their Nanosculpturing by Electron-Beam Irradiation. *Adv. Mater.* **2008**, *20*, 784–787.